Acceleration and localization of subcritical crack growth in a natural composite material

S. Lennartz-Sassinek,* I. G. Main, and M. Zaiser†
School of Engineering and School of Geosciences, University of Edinburgh, Edinburgh, EH9 3JL, United Kingdom

C. C. Graham
Transport Properties Research Laboratory, British Geological Survey, Keyworth, United Kingdom

(Received 15 July 2013; revised manuscript received 14 May 2014; published 12 November 2014)

Catastrophic failure of natural and engineered materials is often preceded by an acceleration and localization of damage that can be observed indirectly from acoustic emissions (AE) generated by the nucleation and growth of microcracks. In this paper we present a detailed investigation of the statistical properties and spatiotemporal characteristics of AE signals generated during triaxial compression of a sandstone sample. We demonstrate that the AE event amplitudes and interevent times are characterized by scaling distributions with shapes that remain invariant during most of the loading sequence. Localization of the AE activity on an incipient fault plane is associated with growth in AE rate in the form of a time-reversed Omori law with an exponent near 1. The experimental findings are interpreted using a model that assumes scale-invariant growth of the dominating crack or fault zone, consistent with the Dugdale-Barenblatt "process zone" model. We determine formal relationships between fault size, fault growth rate, and AE event rate, which are found to be consistent with the experimental observations. From these relations, we conclude that relatively slow growth of a subcritical fault may be associated with a significantly more rapid increase of the AE rate and that monitoring AE rate may therefore provide more reliable predictors of incipient failure than direct monitoring of the growing fault.

DOI: 10.1103/PhysRevE.90.052401 PACS number(s): 46.50.+a, 62.20.mm, 64.60.av

I. INTRODUCTION

For seismologists, physicists, and engineers the nature and causes of the acceleration and localization of damage in natural materials are important outstanding problems. Several empirical laws have been found and theories developed. These include Charles' law, relating crack velocity to the stress intensity factor for tensile laboratory tests [1–3]; the time-reversed Omori law, describing the event (acoustic emission or earthquake) rate prior to large earthquakes, volcanic eruptions, and sample failure in laboratory "creep" tests [4–6]; and the Dugdale-Barrenblatt model for crack growth, incorporating a process (or damage) zone in front of a crack [7], in turn consistent with the scale-invariant fault growth observed in geological systems [8]. In addition, laboratory experiments with acoustic emission (AE) monitoring of samples under compression show strong progressive localization of the acoustic events along an incipient fault plane, associated with a macroscopic strain softening rheology [9]. At the same time, the statistical distribution of AE signatures such as the energy release occurring during individual AE events exhibits power-law statistics indicative of critical dynamic behavior in a complex system, as expressed, e.g., in terms of the well-known Gutenberg-Richter law for AE magnitudes. In this paper, we present a detailed analysis of AE data recorded during triaxial loading of a cylindrical sample of Clashach sandstone, together with a theoretical interpretation of the experimental data, which brings the above-mentioned empirical laws into a single model for the evolution of crack length and AE rate. We first describe some of these empirical relationships in more detail.

In early double torsion experiments [10] with a preexisting notch and guided growth in a cuboid specimen, it was observed that the crack velocity dC/dt is proportional to some power η of the stress intensity factor K (Charles' law),

$$\frac{dC}{dt} \propto K^{\eta}, \tag{1}$$

where η is usually between 20 and 60, for polycrystalline rocks under tension [1–3].

For a constant applied stress, K is proportional to the square-root of the crack length (see, e.g., Ref. [1]), and one obtains from Eq. (1) the differential equation for the (sub-) critical crack length C:

$$\frac{dC}{dt} \propto C^{\eta/2}. \tag{2}$$

Its solution for crack length in the case $\eta > 2$ diverges at a finite time t_f according to Ref. [11]:

$$C(t) = C(0)(1 - t/t_f)^{-\nu}, \tag{3}$$

where $\nu = 1/(\eta/2 - 1)$ is roughly between $1/30$ and $1/10$ for the η range quoted above.

The crack is termed subcritical when the stress applied to the specimen is less than the critical stress required for inducing immediate failure, but above an activation threshold determined by the relevant physiochemical mechanisms governing damage accumulation [12].

A typical time-dependent crack growth curve from Eq. (3), with exponent $\nu = 1/20$, is shown in Fig. 1 (full line). Over a long time the crack grows very slowly until it accelerates very rapidly near the time of failure.

Equations (1)–(3) also hold for rocks under compression [6], albeit with different exponents. The exponent η may

*Current address: Institute for Geophysics and Meteorology, University of Cologne, Cologne, Germany; lennartzsassinek@gmail.com
†Current address: Institute for Materials Simulation WW8, University of Erlangen-Nuremberg, Germany.

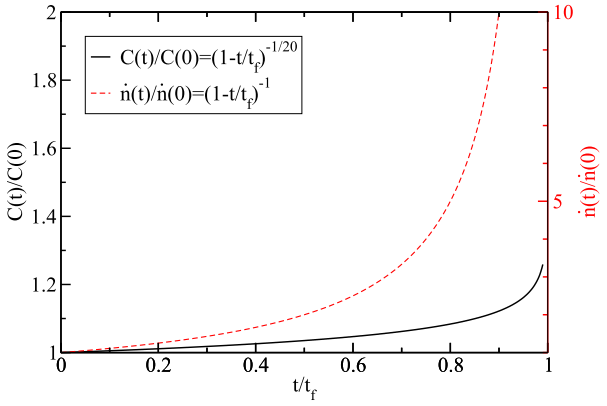

FIG. 1. (Color online) Sketch of a typical evolution of (sub-) critical crack size $C(t)$ (full black line) and event rate $\dot{n}(t)$ (dashed red line) according to Eqs. (3) and (9), respectively; $\nu = 1/20$, time is normalized by the failure time t_f.

in this case be also smaller than 10 leading to ν values larger than $1/4$. It has not yet been possible to measure the crack size directly in those experiments, so this inference is based on indirect measurements of AE.

Here we combine laboratory results with a theoretical model for the damage zone in fracture mechanics in order to relate the time-dependent crack velocity $dC(t)/dt$ to statistical properties of the AE record. AE signals related to fracture processes generally consist of a stochastic sequence of discrete acoustic bursts (henceforth referred to as "events"), which serve as indicators for microscopic damage processes such as microcracking. Owing to its discrete and stochastic nature, the AE signals need to be characterized in terms of statistical properties such as probability distributions and correlations of event amplitudes or interevent times. We analyze in detail the statistical nature of the AE signal and demonstrate that, for our laboratory data, the dynamics of damage accumulation in the run-up to failure as reflected by the AE signal can be well described in terms of average signatures such as event numbers and AE rates.

We demonstrate that failure is preceded by a characteristic acceleration of the AE rate and concomitant increased spatial clustering and localization of the AE events on a quasiplanar zone of damage accumulation, which can be considered as an incipient fault plane. We make the assumption that the characteristic extension of the fault zone controls failure in a similar manner as the length of a critical crack does in the context of fracture mechanics (for detailed discussion of this point see Ref. [13]). This allows us to relate the crack size to the number of AE events and to use the AE record for monitoring damage accumulation and predicting time-to-failure even when it is impossible to measure the crack size directly within an experiment.

II. EXPERIMENT

The AE data described in the following section were recorded during the triaxial loading of a cylindrical sample of Clashach sandstone (105 mm in length and 50 mm in diameter) [14]. A detailed description of the sample material and the experimental setup is given in Ref. [15]. The sample was subjected to a pore-fluid pressure of 10.5 MPa (with deaired water) and a confining pressure of 50.5 MPa (provided by hydraulic oil). A rubber jacket was used to isolate the sandstone from the confining fluid (hydraulic oil), through which an array of 18 piezoelectric transducers (PZT) were emplaced inside brass housings, with a further two sensors embedded within the pistons. A total of 12 P-wave PZTs and 8 S-wave PZTs were utilized for this test, while five of the P-wave sensors also acted as transmitters for a regular ultrasonic pulse (every minute), thereby allowing the changing ultrasonic velocity field to be monitored within the sample. The sample was loaded at a constant axial strain rate of 1.7×10^{-6} s^{-1}, until failure occurred by shear localization. A brief period of strain-softening was observed before an abrupt stress drop indicating sample failure. The acoustic waveforms generated from the test were preamplified, then recorded by a 12-channel transient recording system (DaxBox, Prökel GmbH, Germany) at a sampling rate of 10 MHz. P-wave arrival times were automatically picked by an algorithm utilizing the approach of Leonard and Kennett (1999) [16]. Where AE were detected at a minimum of eight sensors, hypocenter locations were then also determined automatically, using a downhill simplex algorithm [17], which allows for temporal changes in the velocity field. The resulting hypocenters were located with an uncertainty of ± 1 mm, and the locations, initiation times, as well as the amplitudes of these events were recorded.

The resulting sequence of about 25 000 AE events is used here to characterize the damage processes occurring in the run-up to sample failure. The AE sequence is characterized by acceleration of the AE rate as indicated by decreasing interevent times (defined as the difference between the initiation times of two sequential events), accompanied by increasing localization of events in the vicinity of an incipient failure plane.

III. STATISTICAL ANALYSIS OF THE AE RECORD

A. Spatial localization

To characterize the spatial structure of the AE pattern, we define the failure plane as the plane for which the mean-square separation between that plane and the locations of the last 5 000 events is minimum. We also define an associated damage zone around that plane, as described below.

Figure 2(a) shows the histogram of event distances to the failure plane for five subsequent subsets of the AE sequence. One can see clearly that with increasing event number the AE events increasingly localize within the damage zone defined above. Figure 2(b) shows for two subsets of events ($i =$ 12 000–17 000 and $i =$ 20 000–25 000) the spatial distribution of these events projected on a cross-section where the failure plane corresponds to the plane $z = 0$ and the specimen axis is contained in the xz plane. One can clearly see that most of the last 5 000 AE events (69%) locate within 2.5 mm of the eventual fault or failure plane. We use this metric from Fig. 2(a) to define the damage zone shown by the red (dark gray) lines in Fig. 2(b). The opposite holds for the earlier subsets, where events are distributed more evenly throughout the sample. These data confirm that deformation becomes progressively more localized during the experiment.

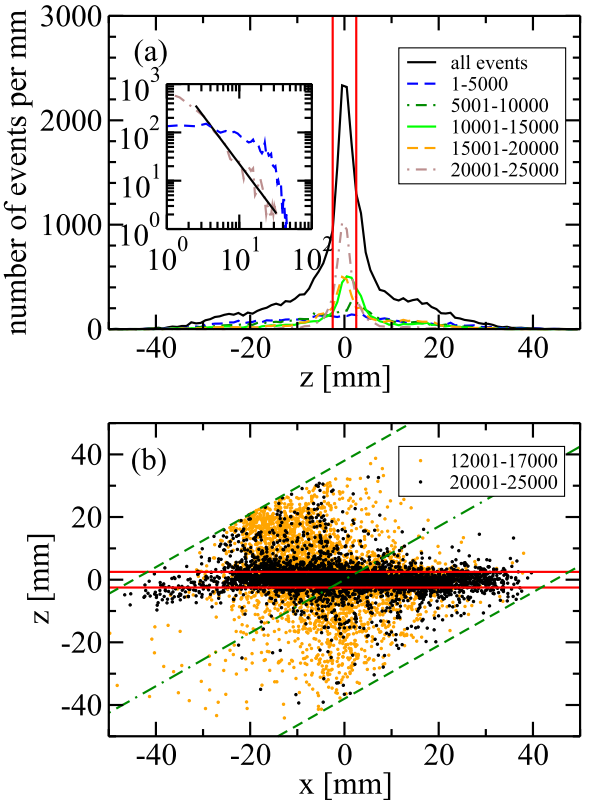

FIG. 2. (Color online) (a) Histogram of the perpendicular distances of the event locations to the final failure plane for different subsequences of the record. The inset shows the curves for the first and last 5 000 events in a double logarithmic presentation. The black straight line is a reference curve with a power law exponent of −2. (b) Location of acoustic emissions (dots), projected onto a cross-section of the the x-z plane, where $z = 0$ defines the eventual fault plane. Events numbered $i = 12\,000$–$17\,000$ are indicated in dark yellow (grey) and $i = 20\,001$–$25\,000$ in black. In both plots the red (dark gray) lines indicate the damage zone of width ±2.5 mm around the failure plane. The green dashed lines in plot (b) indicate the boundary and the green dash-dotted line indicates the middle axis of the specimen, which is also the direction of the applied stress.

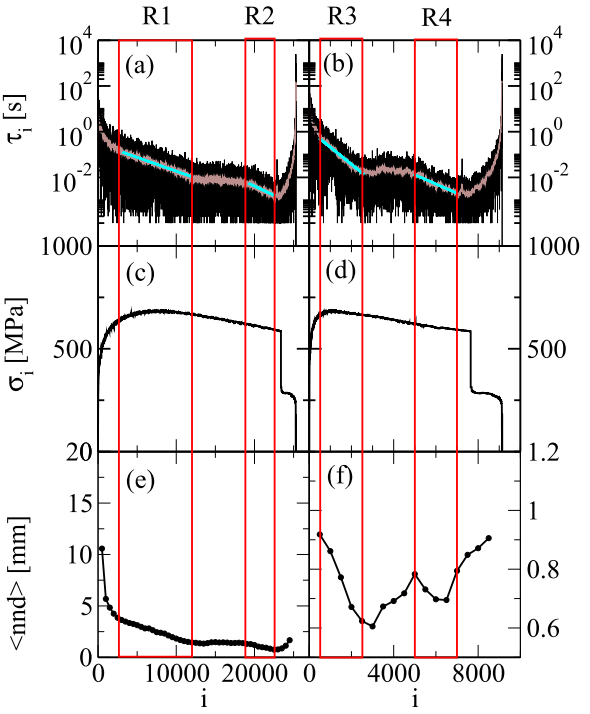

FIG. 3. (Color online) Evolution of various experimental parameters as a function of the AE event number i; on the left-hand side, event number refers to all events; on the right-hand side, only events located within the damage zone surrounding the final failure plane are counted. (a) and (b) Interevent times: black, all interevent times τ_i; brown (gray), interevent times averaged over windows of 50 events; in the regions R1–R4, marked by red (dark gray) boxes, the interevent times can be fitted by exponential functions. (c) and (d) Differential stress σ_i in units of MPa. (e) and (f) Average spatial separation of nearest neighbor events (mean nearest-neighbor distance, ⟨nnd⟩), evaluated over a moving window of 1 000 events.

The inset in Fig. 2(a) quantifies this further, showing that in the first part of the test the events are located more or less randomly through the sample, with a flat distribution of distances of AE events from the nearest point on the best-fitting incipient fault plane, curving over in the tail due to the finite sample boundaries. In contrast, the data for the last part of the test is consistent with an emergent power-law distribution of exponent −2. For natural seismicity this exponent is −1.35 [18]. The difference between the exponents is likely due to the fact that the latter measure takes no account of the finiteness of the fault plane and is largely based on "aftershock"-type triggering, including the susceptibility of nearby preexisting critically stressed faults to small triggering stresses, rather than the precursory localization on an incipient fault observed here. To assess the influence of the observed spatial localization on the event statistics, we will conduct two parallel analyses (a) for all events irrespective of location and (b) for the events contained within the damage zone.

Figures 3(a) and 3(b) show the observed interevent times as a function of the event number i, (a) for all events and (b) restricted to the events contained within the damage zone. To enable connection with the mechanical response of the sample, Figs. 3(c) and 3(d) show the differential stress applied during the experiment, also as a function of the event number. When interpreting this figure it is important to note that, even though events are temporally ordered, the event number i should not be considered a simple proxy for time. The interval of near-linear stress increase at the beginning of the test accounts for a significant fraction of the test duration but comprises only a relatively small number of AE events. On the other hand, the majority of events occur during the softening regime, where the stress slightly decreases from the peak to the failure stress, leading to only minor stress differences over most of the events. This strain softening phase encompasses only about 5% of the test duration but contains most of the AE events. Localization around the incipient plane occurs at or near the peak stress [$5\,000 < i < 10\,000$ in Fig. 2(a)]. As a consequence, practically all events in the damage zone occur during the softening regime [Fig. 2(b)]. Failure is marked by a large load drop, after which some AE activity continues at a much reduced stress level.

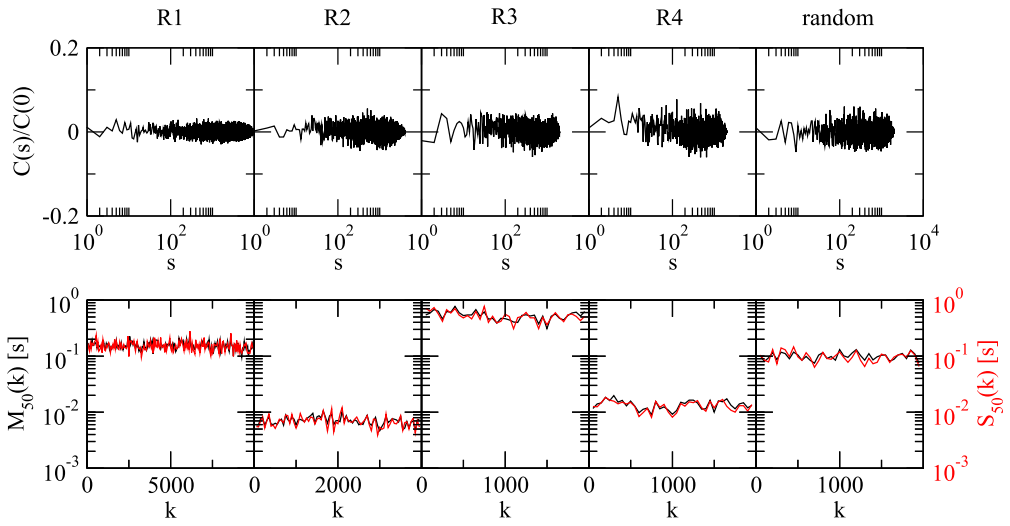

FIG. 4. (Color online) Signatures of the scaled interevent time statistics in the different exponential relaxation regimes: top row, covariance of interevent times separated by s events; bottom row, mean scaled interevent time $M_{50}(k)$ (black) and standard deviation $S_{50}(k)$ [red (gray)], evaluated over disjoint windows of 50 events starting at event k. The last column shows the results for random surrogate data (2000 time values drawn independently from an exponential distribution with mean value 0.1 s).

Figures 3(a) and 3(b) demonstrate that the interevent times exhibit significant statistical scatter; however, the underlying trend is that they tend to decrease with increasing event number. To make the trend more visible, we average the interevent times τ_i over a moving window of 50 events; i.e., we replace τ_i by the average of all $\tau_j, j \in [i-24, i+25]$ [brown (gray) data points in Fig. 3]. From these data one can identify in each graph two regimes where the averaged interevent times decrease with increasing event number in an approximately exponential manner. During the two regimes of exponential decrease, identified by straight lines on Fig. 3, the spatial distribution of damage is different from that during the intervening interval where the interevent time remains roughly constant. During both exponential decreasing regimes, the majority of events are located within the damage zone surrounding the final failure plane, but a different behavior is observed during the intervening interval: During this latency period, most AE events are located within a second zone of coalescent damage [15] that emerges outside the damage zone and which we could identify as a conjugate fault plane. The different spatial structure of the AE patterns in both cases can be clearly seen in Fig. 2(b), where events accumulating during the latency period are shown in dark yellow (gray).

B. Statistics of interevent times

To analyze the statistical properties of the random process τ_i in the exponential relaxation regimes, we separately consider each of the regimes R1–R4 evident in Fig. 3. For each we define a relaxation coefficient a as the slope of the least-square fit of a linear function to the data points $[i, \ln(\tau_i)]$. For the record of all events irrespective of location [black data shown in Fig. 3(a)], this gives the values $a = 0.00028$ for R1 and $a = 0.00029$ for R2. For the record of events centered around the final failure plane [black data shown in Fig. 3(b)], the corresponding values are $a = 0.0017$ (R3) and $a = 0.000094$ (R4).

We now are in a position to remove the trend by defining the scaled variable $\tilde{\tau}_i = \tau_i \exp(ai)$. Because of the different a values we do this for each of R1–R4 separately. Furthermore, we use the counting convention that i is set to 1 for the first event of each regime. Figure 4 (top) shows the covariance $C(s) = \langle \tilde{\tau}_i \tilde{\tau}_{i+s} \rangle - \langle \tilde{\tau}_i \rangle^2$, averaged over all i and normalized by $C(0)$. For all four exponential relaxation regimes it is evident that up to statistical fluctuations due to finite sample size, the covariance is for all s close to zero. Hence, we will in the following envisage $\tilde{\tau}_i$ as an uncorrelated random process. We next consider the mean $M_l(k)(\tilde{\tau}) = \langle \tilde{\tau}_i \rangle_{k \ldots k+l}$ and variance $V_l(k)(\tilde{\tau}) = \langle \tilde{\tau}_i^2 \rangle_{k \ldots k+l} - \langle \tilde{\tau}_i \rangle^2_{k \ldots k+l}$, which we evaluate over disjoint intervals $i \in [k \ldots k+l]$ of length l. Figure 4 (bottom) shows the mean $M_{50}(k)$ and standard deviation $S_{50}(k) = V_{50}(k)^{1/2}$ as a function of k. Up to statistical fluctuations, no discernible trend can be observed. For comparison, we have also included $C(s)$, $M_{50}(k)$, and $S_{50}(k)$ as evaluated for random and uncorrelated surrogate data (2 000 time values drawn independently from an exponential distribution with average 0.1 s). We finally note that for $2 \leqslant l \leqslant 256$), the variance of the mean is found to be related to the mean variance by $\langle M_l(k)^2 \rangle_k - \langle M_l(k) \rangle_k^2 \approx (1/l) \langle S_l(k) \rangle_k$, as expected for a stationary and uncorrelated random process.

It is evident from Fig. 4 that the mean of $\tilde{\tau}_i$ is approximately equal to the standard deviation. To understand the reason for this, we determine the probability distribution of $\tilde{\tau}_i$, shown in Fig. 5. It is evident that, for all four regimes, the scaled interevent times are exponentially distributed—which means that the coefficient of variation (the ratio of the standard deviation and the mean) is equal to unity. Moreover, if we split the data into sequential subsequences and determine distributions for these separately, it is seen that the distributions for the subsequences are identical, again confirming the stationarity of the scaled process. Based on the evidence in Figs. 4 and 5, we will in the following consider $\tilde{\tau}_i$, in each exponential relaxation regime, as a stationary, uncorrelated random process with exponential frequency distribution.

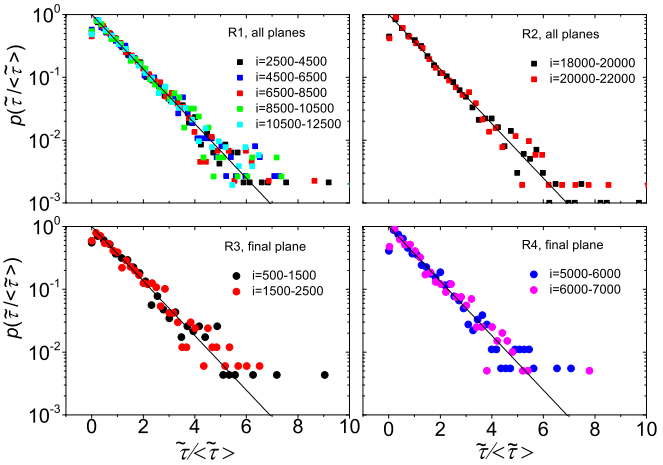

FIG. 5. (Color online) Statistics of the scaled interevent times $\tilde{\tau} = \tau \exp(ai)$ for the different exponential relaxation regimes R1–R4; the corresponding mean values are $\langle\tilde{\tau}\rangle = (0.052 \pm 0.0008)$ s for R1, $\langle\tilde{\tau}\rangle = (0.0071 \pm 0.00011)$ s for R2, $\langle\tilde{\tau}\rangle = (0.536 \pm 0.011)$ s for R3, $\langle\tilde{\tau}\rangle = (0.0036 \pm 0.00014)$ s for R4.

C. Statistics of event accumulation

Our analysis of the record of interevent times has demonstrated that the series τ_i can be considered the product of an uncorrelated random process $\tilde{\tau}_i$ and an exponential decrease $\exp(-ai)$ of the mean interevent time with increasing event number. To understand the consequences for the event accumulation process, we evaluate the occurrence time t_n of event number n. This is given by the sum of all interevent times up to τ_n:

$$t_n = \sum_{i=1}^{n} \tau_i = \sum_{i=1}^{n} \exp(-ai)\tilde{\tau}_i. \tag{4}$$

Using the statistical properties of the process $\tilde{\tau}$ we can calculate the mean and variance of the occurrence times. We obtain

$$\begin{aligned} \langle t_n \rangle &= \frac{\langle\tilde{\tau}\rangle}{a}[1 - \exp(-an)] + \mathcal{O}(a^0), \\ \left\langle t_n^2 \right\rangle - \langle t_n \rangle^2 &= \frac{\langle\tilde{\tau}\rangle^2}{2a}[1 - \exp(-2an)] + \mathcal{O}(a^0), \end{aligned} \tag{5}$$

where we have used in the last step that the variable $\tilde{\tau}$ is exponentially distributed, hence its mean and standard deviation are equal. In these equations, $\langle\tilde{\tau}\rangle$ can be understood as the expected interevent time at the moment in time when we start counting. The expected time-to-failure from this point is obtained by setting $n \to \infty$, $t_f = t_\infty$. We find that, up to terms of higher order in a,

$$\langle t_f \rangle = \frac{\langle\tilde{\tau}\rangle}{a}, \quad \frac{\left\langle t_f^2 \right\rangle - \langle t_f \rangle^2}{\langle t_f \rangle^2} = \frac{a}{2}. \tag{6}$$

If we want to study the statistical properties of the counting process $n(t)$, which gives the number of events that have occurred at a given time t, we encounter a problem: Unlike standard counting processes such as a Poisson process where events occur at fixed rate, here the event rate increases exponentially with event number. As seen from Eq. (5), this implies that the event time for $n \to \infty$ reaches an asymptote t_∞ (the failure time), which itself is statistically distributed, with mean and standard deviation given by Eq. (6). At this failure time, which is different for different realizations of the event accumulation process, the event number diverges. If we now investigate an ensemble of different realizations of the process $\{\tau_n\}$ and the associated process $\{t_n\}$ in order to study the time-dependent statistics of event numbers, we encounter a problem: As we approach the expected failure time, more and more members of the ensemble will have failed $[n(t) = \infty]$, and it is therefore not possible to calculate statistical moments $\langle[n(t)]^k\rangle$ in a meaningful manner.

This problem can be solved by evaluating moments of n not at fixed values of t, but at fixed values of (t/t_f) where t_f is the failure time for the realization of $\{\tau_n\}$ under consideration, and hence is different for each member of the ensemble. Using this type of conditional statistics, it is evident by construction that all members of the ensemble fail at $t/t_f = 1$, and that meaningful statistical information can be gathered for all values of $t/t_f < 1$. In terms of ensemble statistics, this implies that we do not consider an ensemble of systems at fixed times, but at fixed relative distance to their respective failure times.

For illustration, we have performed simulations of event accumulation using 1 000 realizations of $\{\tau_n\}$, each consisting of a sequence of $N = 10^5$ events with interevent times $\tau_i = \tilde{\tau}_i \exp(-ai)$ where $a = 3 \times 10^{-4}$ and $\tilde{\tau}_i$ is drawn independently from an exponential distribution with mean value $\langle\tilde{\tau}_i\rangle = 1$ (since we will divide times by the failure time, the unit is irrelevant). We calculate for each sequence the occurrence times $\{t_i\}$ for all events as well as the sample-specific failure time t_f. This time is estimated from t_N by approximating the residual time by its expectation value according to Eq. (6): $t_f \approx t_N + \exp(-aN)/a$, where $\exp(-aN)$ is the mean interevent time after N events. We then determine for each sample the values of $n(t/t_f)$ at fixed values of t/t_f and calculate their mean and standard deviation. The results are shown in Fig. 6. Within the plotting resolution the mean values follow, on the single-logarithmic plot, exactly a straight line. To understand the origin of this functional form we replace Eq. (4) by its

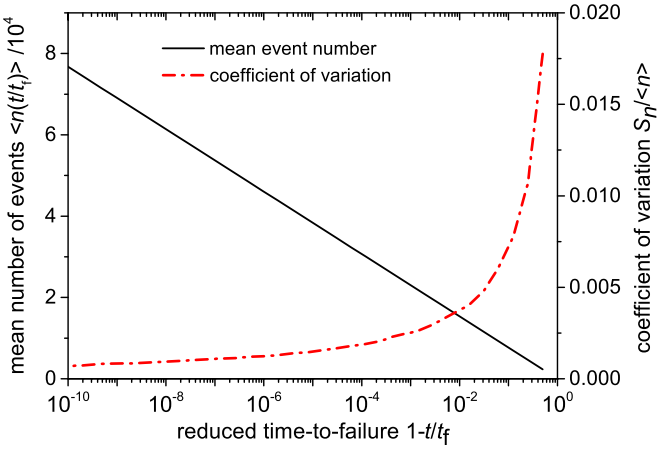

FIG. 6. (Color online) Black solid curve, evolution of the mean event number n as a function of time-to-failure t/t_f; the straight line on the semilogarithmic plot follows exactly the prediction of Eq. (8); red dash-dotted curve, coefficient of variation of n.

deterministic counterpart,

$$t(n) = t_f[1 - \exp(-an)], \tag{7}$$

and invert this equation to obtain

$$n(t) = \frac{1}{a} \ln\left[\left(1 - \frac{t}{t_f}\right)^{-1}\right]. \tag{8}$$

Also shown in Fig. 6 is the coefficient of variation of $n(t)$ as evaluated from the ensemble simulation. This coefficient is small and decreases to zero for $t/t_f \to 1$. As a consequence, the statistical sampling error on the $n(t/t_f)$ plot, as well as the scatter of the plotted points around the prediction of Eq. (8), is within the thickness of the straight line for all points plotted. Thus, we may consider Eq. (8) as asymptotically exact in the vicinity of the failure time and as a very good approximation elsewhere. This allows us in the following to consider damage accumulation, despite the very significant fluctuations of the interevent times, in fundamentally deterministic terms.

Some caution is, however, required when using Eq. (8) to predict event numbers: Since the failure time t_f in this equation must be envisaged as a stochastic variable that differs from sample to sample, Eq. (8) should not be used for making predictions of the event number at future times that are close to the mean failure time $\langle t_f \rangle = \langle \tilde{\tau} \rangle / a$. Rather, Eq. (8) describes how the AE event number increases for a given sample as time approaches the sample-specific failure time t_f.

D. Statistics of AE amplitudes

To characterize the statistics of AE amplitudes m, the sequence of all events was again divided into subsequences containing 2 000 events each, and probability distributions of m were determined separately for each subsequence. A similar procedure was adopted for the events contained within the damage zone around the failure plane, where subsequences of 1 000 events were considered.

The probability distributions are, for events above the mean amplitude, well characterized by an exponential decay, $p(m) \propto 10^{-bm}$ with an exponent of $b \approx 0.7$ (full lines in Fig. 7). If the amplitudes are scaled by their mean values in the respective subsequence (and even without that, since the mean amplitudes do not change significantly), all distributions fall on top of each other. There is no significant difference

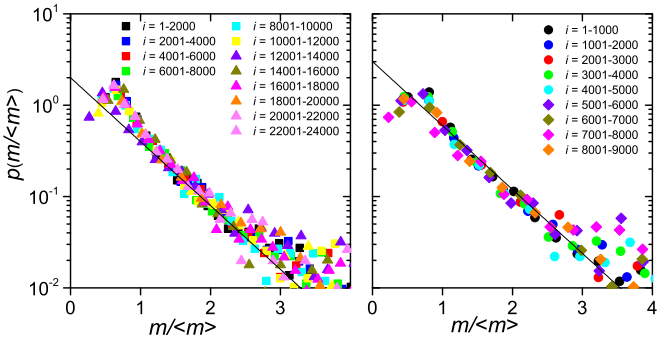

FIG. 7. (Color online) Distributions of event amplitudes for different AE event subsequences; the right graphs represent events contained within the damage zone. All amplitudes have been normalized by the mean values for the respective subsequence.

between the amplitude distributions for all events and those which consider only events contained in the damage zone, or between the distributions early in the failure sequence and those closer to the point of macroscopic failure.

While there is a pronounced acceleration of the AE rate, the mean AE amplitude remains practically unchanged in the run-up to failure, rising sharply only in the last second or so (shown in top graphs of Fig. 8).

IV. DAMAGE ACCELERATION, SPATIAL CLUSTERING, AND CRACK GROWTH

We have shown that, in the vicinity of the specimen-specific failure time t_f where $t_f \approx \langle \tilde{\tau} \rangle / a$, the event number diverges according to Eq. (8), which predicts that near failure the number $n(t)$ diverges as the logarithm of an inverse power law. From Eq. (8) it follows that the characteristic event rate diverges like

$$\dot{n}(t) = \frac{dn}{dt} = \frac{1}{t_f a}(1 - t/t_f)^{-1}. \tag{9}$$

Equation (9) corresponds to the reverse-time Omori's law sometimes seen in natural seismicity, also with an exponent $-p$ near -1 [8,19–22]. A plot of Eq. (9) for the event rate evolution is shown on Fig. 1 (dashed red line) for comparison with the crack growth curve of Eq. (3), with both parameters normalized to their starting values. The comparison indicates that monitoring the event rate may provide earlier and more sensitive indicators of approaching failure than direct monitoring of the crack length or, more generally, the damage pattern. This may explain why microearthquake event rate is often used pragmatically as a strong metric in operational forecasting of volcanic eruptions and underground mining collapses and rock bursts, for example.

We first attempt a direct comparison of the observed event rate with the values evaluated using Eq. (9), with $t_f = 6240.7$ s identified with the time from the start of the experiment to the macroscopic load drop seen in Figs. 3(c) and Fig. 3(d). To this end, we evaluate the event rate over a moving window of length $l = 50$ as $\dot{n}_l(k) = l/\Delta t_l(k)$, where $\Delta t_l(k) = \sum_{i=k}^{k+l} \tau_i$, and the corresponding time $t_l(k) = t_k + \Delta t_l(k)/2$, where t_k is the occurrence time of event k.

A direct comparison between Eq. (9) and the $[\dot{n}_l(k), t_l(k)]$ data does not work well since the experimental event rate exhibits a "hiatus," which is inconsistent with a power-law increase (black curves in Fig. 8). This feature coincides with the intervening time interval $[t_1, t_2]$ with $t_1 = 6179$ s and $t_2 = 6228$ s, corresponding to the AE with event numbers 12 500 and 19 100 of the complete record. During this time interval a second damage zone is active and the acceleration of the event rate is interrupted (Figs. 2 and 3). If we remove this time interval from the analysis and shift the apparent failure time $t_f' = t_f - (t_2 - t_1)$ for the antecedent events accordingly, then both the event rates prior to this confounding interval (first exponential acceleration regime) and those after the confounding interval (second exponential acceleration regime) are well represented by Eq. (9), as can be seen from the green (light gray) and blue (dark gray) curves in Fig. 8.

In particular, the data pertaining to the damage zone surrounding the final failure plane match the prediction of

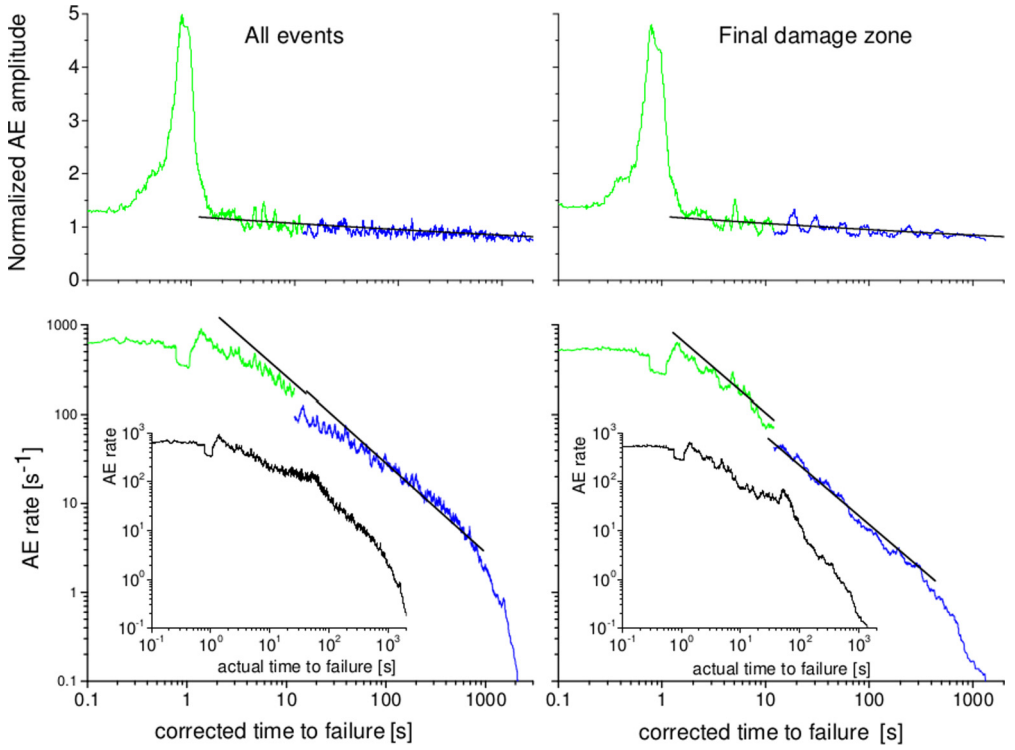

FIG. 8. (Color online) Top: evolution of event amplitude in the run-up to failure; left, all events; right, only events in damage zone around final failure plane; all amplitudes have been normalized by the average amplitude over all events. Bottom: evolution of event rate in the run-up to failure; left, all events; right, only events in damage zone around final failure plane; black curves, raw data; green (light gray) curves, data pertaining to second acceleration regime; blue (dark gray) curves, data from first acceleration regime with shifted failure time $t_f' = t_f - (t_1 - t_2)$; black lines in the top figures, Eq. (3) with AE amplitude $\propto C$ and $\nu = 1/20$; black straight lines in the bottom figures, Eq. (9).

Eq. (9), with the parameter a taken from the fit to the exponential acceleration regime, extremely well. This implies that acoustic emissions associated with localization on the ultimate fault plane are temporarily stabilized or switched off while deformation shifts to an alternate plane. When the process restarts on the first plane it retains a strong memory of the previous history. This memory effect is well known in acoustic emission studies involving controlled external stress relaxation and is known as the "Kaiser effect" [23,24]. To our knowledge this is the first time the Kaiser effect has been seen as a consequence of emergent internal stress redistribution within a deforming sample.

We can also see that the reverse Omori law ceases to hold within the last second of the failure sequence. During this time interval, a reduction in the event rate is accompanied by a drastic and sudden increase in the event amplitude (top graphs in Fig. 8). This is associated with an increase in the mean event size and is most likely due to "masking" of smaller events by longer and larger events that begin to overlap in time. The dynamic behavior in the final second is complex and cannot be explained in a simple way by the quasistatic theory presented here.

We now consider the implications of our findings for the dynamics of damage accumulation in the failure plane and investigate to what extent this can be envisaged as a coherent crack propagation and growth process. Taking Eq. (3) together with Eq. (9) yields for the velocity of subcritical crack growth

$$\dot{C}(t) = \frac{dC}{dt} = \frac{\nu C(0)}{t_f}(1 - t/t_f)^{-\nu-1} = \nu a C(t)\dot{n}(t), \tag{10}$$

where $C(t)$ is the length of the macroscopic crack or growing fault. To interpret this equation, we recur to the concept of scale-invariant crack growth [25] as established in fracture mechanics: For an elastic material, linear elastic fracture mechanics states that ahead of a crack of length C the material is elastically deformed under a stress that decays according to $\sigma \propto \sqrt{C/r}$ with distance r from the crack tip [1,12,26,27]. But real materials are not ideally elastic: within a zone where σ exceeds the yield stress of the material (thus within a radius proportional to the crack length) plastic deformation occurs (Dugdale-Barrenblatt model [7]) in the form of an increasing number of micro cracks. This zone is called process zone or damage zone and also appears in natural fault growth [25]. Scale-invariant crack growth thus simply means that the extension of the "damage zone" where damage accumulates around the tip of a growing crack is proportional to the length of the crack. Equation (10) follows from this idea if we make the assumptions that (i) crack growth occurs by the same damage accumulation processes that cause acoustic emission and that (ii) the amount of damage corresponding to a single AE event is proportional to the

extension of the damage zone, hence to the crack length. It then follows that the crack growth rate is proportional both to the crack length and to the AE event rate, as stated by Eq. (10).

The idea that the damage per event is proportional to the crack length is supported by studying the increase of the mean AE amplitude, which we may use as as a proxy for the mean amount of damage per AE event. By fitting Eq. (3) to the AE amplitude increase we find, in the regimes where Eq. (9) is expected to hold, a small exponent $\nu \approx 1/20$ [black curves in Fig. 8(top)]. With such small ν, Eq (10) is consistent with the observation of similar Charles' law exponents for event rate and crack growth rate in double torsion tensile tests [2]. Equation (10) thus unifies the outcome of Charles' law for subcritical crack growth [Eq. (3)] with the time-reversed Omori law with exponent 1 [Eq. (9)] and scale-invariant crack growth into a single model.

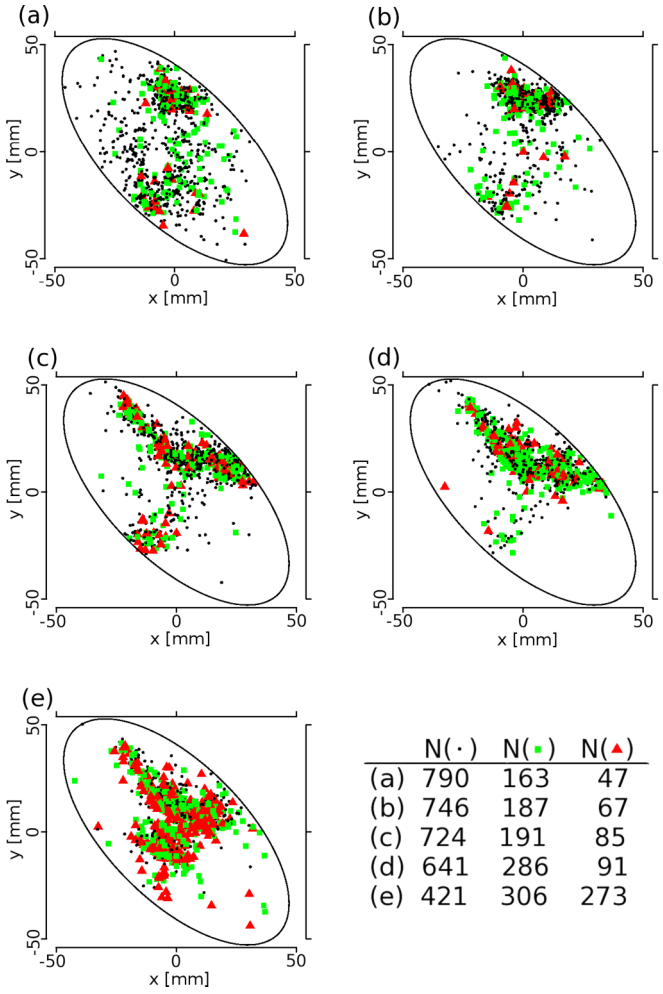

	N(·)	N(▪)	N(▲)
(a)	790	163	47
(b)	746	187	67
(c)	724	191	85
(d)	641	286	91
(e)	421	306	273

FIG. 9. (Color online) Plan view of the final failure plane of the Clashach sandstone specimen. The symbols indicate the location of acoustic emissions measured around the final plane for (a) events 500–1 500, (b) 1 500–2 500, (c) 5 000–6 000, (d) 6 000–7 000, and (e) 6 500–7 500. Events with small amplitudes ($m/\langle m\rangle \leqslant 1.1$) are indicated by circles, medium-sized events ($1.1 < m/\langle m\rangle \leqslant 2.2$) are indicated by squares, and triangles indicate events with large amplitudes ($2.2 < m/\langle m\rangle$).

Equation (10) implies that the crack is growing exponentially with respect to the event number:

$$C(n) = Be^{bn}, \tag{11}$$

with $b = \nu a$. If we take the measured values 0.00028–0.0017 for the parameter a, and the typical value of $\nu = 1/20$, the parameter b is of the order of 10^{-5}–10^{-4}). Therefore, for $\Delta n = 1\,000$, the relative increase of the crack size, $\Delta C(n,\Delta n)/C(n) = (e^{b\Delta n} - 1) \approx 0.01$–$0.1$, is very small. Again, this is consistent with the experimental observations of a slowly growing crack front associated with the slow movement of a crescent-shaped "process zone," in turn inferred from the evolution of AE locations in Fig. 9. The zone of clustered damage increased only slightly with respect to event number as expected from Fig. 1 until very near the failure time.

As C changes only slowly with n, it follows from Eq. (10) that event rate is a good indicator of crack velocity. This is consistent with Fig. 1: Since the two exponents for C and dn/dt differ by about 1, those for dC/dt and dn/dt are approximately equal. In practical terms, measuring event rate is much easier than attempting to directly measure the crack velocity from time-lapse images of AE locations, which represent a diffuse pattern from which it is difficult to locate the extension of the crack or fault zone.

V. DISCUSSION AND CONCLUSIONS

For guided tensile cracks we can derive the inverse power-law acceleration-to-failure of variables such as crack growth rate and energy release rate directly from the observation of controlled stress intensity and the resultant crack velocity. Here we show for the case where a fault is growing in a compressive stress field that experimental observations of the AE event rate show an inverse power-law acceleration, which, in combination with the theory of the damage zone in fracture mechanics, indicates self-similar growth of the dominant fault with respect to the event rate as the total number of events within the final failure plane increases according to the logarithm of an inverse power law with time. This corresponds to an exponential growth with respect to the event number. The model is consistent with simultaneous observation of relatively slow crack growth (small exponent ν) and much more rapid increase in AE rate (exponent $p = 1$).

It is interesting to discuss our findings in terms of their implication for forecasting failure based upon the recorded AE. Localization of damage on an incipient failure plane occurs early in the run-up to failure, but direct monitoring of the spatial distribution of damage in the vicinity of this plane gives little forewarning owing to the slow growth and sudden acceleration of the incipient fault. A more promising approach is to focus on the interevent times and use the AE record to derive statistical estimates of the exponential acceleration coefficient a and the mean scaled interevent time $\langle\tilde{\tau}\rangle$, from which an estimate of the remaining time-to-failure follows according to Eq. (6). Using a least-square fit of a linear function $x_i = b - ai$ to the values of $x_i = \ln\tau_i$ gives, for a sequence of $l = 1\,000$ interevent times, a typical statistical error of 10% for a. The value of $\langle\tilde{\tau}\rangle$ follows for the same event sequence as $\langle\tilde{\tau}\rangle = \langle\tau_i \exp(a_i)\rangle$ with a typical statistical accuracy of $1/\sqrt{l}$. We can then estimate the time-to-failure

TABLE I. Failure time predictions based upon Eq. (6).

	R1, all events	R2, all events	R3, events near failure plane	R4, events near failure plane
Analyzed events	$i = 2500$–4500	$i = 19000$–21000	$i = 500$–1500	$i = 5000$–6000
Start time t_s	5661 s	6227.4 s	5873 s	6226.9 s
End time t_e	5896 s	6235.9 s	6140 s	6235.8 s
Estimated a	$(3.16 \pm 0.4) \times 10^{-4}$	$(3.53 \pm 0.4) \times 10^{-4}$	$(17.3 \pm 1.4) \times 10^{-4}$	$(11.5 \pm 1) \times 10^{-4}$
Estimated $\langle\tilde{\tau}\rangle$	(0.159 ± 0.006) s	(0.0059 ± 0.0002) s	(0.575 ± 0.02) s	(0.0152 ± 0.0007) s
Predicted time to failure $t_f - t_s$	(503 ± 85) s	(16.7 ± 2.4) s	(332 ± 34) s	(13.2 ± 2.1) s
Actual time to failure $t_f - t_s$	579 s	12.6 s	367 s	12.7 s
Corrected time to failure $t'_f - t_s$	530 s	12.6 s	328 s	12.7 s

from the start of the sequence as $t_f \approx \langle\tilde{\tau}\rangle/a$ with a typical error of $\Delta t_f/t_f \approx \Delta a/a + 1/\sqrt{l} + \sqrt{a/2}$, where the last term is the intrinsic statistical scatter of t_f for given $\langle\tilde{\tau}\rangle$ and a. Typical values of the overall error of t_f as estimated for a sequence of 1 000 events are of the order of 15%, of which the intrinsic scatter $\sqrt{a/2}$ accounts only for 1–3%. This demonstrates that the quality of predictions is limited mainly by the accuracy of estimates of the parameters $\langle\tilde{\tau}\rangle$ and a obtained from a limited record.

Examples of predictions based on subsets of the four acceleration regimes R1–R4 are compiled in Table I. We can see that the accuracy of the prediction improves as we approach the true failure time, in such a manner that the relative error of the prediction remains approximately constant. Predictions based upon analysis of events in the vicinity of the incipient failure plane perform better than predictions which use all events; however, it may in practice be difficult or even impossible to identify the failure plane at an early stage of the damage accumulation process. Finally, we note that predictions using data from regimes R1 and R3 are biased by the presence of a quiescent interval where the acceleration to failure is interrupted by the activation of a second, conjugate fault zone where most of the AE activity localizes for about 50 s. During this time interval, the final fault becomes inactive but the acceleration resumes unchanged after AE activity returns to the initial plane, implying significant memory retention in the reactivation process. It is obvious that, while such confounding effects can be easily identified in a postmortem analysis, they may have significant impact on the accuracy of real time predictions, which in the present case, if based on the first acceleration sequence, would have led to a predicted failure time that is approximately 50 s too early.

ACKNOWLEDGMENTS

This work was supported by EPSRC under Grant No. EP/I018492/1 within the framework of the ERA-Net Complexity-Net project LOCAT.

[1] B. K. Atkinson and P. G. Meredith, in *Fracture Mechanics of Rock*, edited by B. K. Atkinson, (Academic Press, Londonx, 1987), pp. 111–166.
[2] P. G. Meredith and B. K. Atkinson, Geophys. J. R. Astr. Soc. **75**, 1 (1983).
[3] I. G. Main, P. R. Sammonds, and P. G. Meredith, Geophys. J. Int. **115**, 367 (1993).
[4] I. G. Main, Geophys. J. Int. **139**, F1 (1999).
[5] I. G. Main, Geophys. J. Int. **142**, 151 (2000).
[6] N. Brantut, P. Baud, M. J. Heap, and P. G. Meredith, J. Geophys. Res. **117**, B08412 (2012).
[7] G. I. Barenblatt, Adv. Appl. Mech. **7**, 55 (1962).
[8] Y. Y. Kagan and L. Knopoff, Geophys. J. R. Astron. Soc. **55**, 67 (1978).
[9] D. A. Lockner, J. D. Byerlee, V. Kuksenko, A. Ponomarev, and A. Sidorin, Nature **350**, 39 (1991).
[10] B. K. Atkinson, J. Geophys. Res. **89**, 4077 (1984).
[11] S. Das and C. H. Scholz, J. Geophys. Res. **86**, 6039 (1981).
[12] B. Lawn, *Fracture of Brittle Solids*, 2nd ed. (Cambridge University Press, Cambridge, 1993).
[13] S. Lennartz-Sassinek, M. Zaiser, I. G. Main, C. Manzato, and S. Zapperi, Phys. Rev. E **87**, 042811 (2013).
[14] We thank Georg Dresen and Sergei Stanchits. The experiment has been carried out in their laboratory at the Deutsches Geoforschungszentrum (GFZ) in Potsdam, Germany.
[15] C. C. Graham, Ph.D. thesis, University of Edinburgh, Edinburgh, United Kingdom, 2010, http://hdl.handle.net/1842/4654.
[16] D. A. Leonard and B. L. N. Kennett, Phys. Earth Planet. Inter. **113**, 247 (1999).
[17] J. A. Nelder and R. Mead, Comput. J. **7**, 308 (1965).
[18] K. Feltzer and E. Brodsky, Nature **441**, 735 (2006).
[19] S. Hainzl, G. Zöller, and J. Kurths, J. Geophys. Res. **104**, 7243 (1999).
[20] L. M. Jones and P. Molnar, J. Geophys. Res. **84**, 3596 (1979).
[21] B. C. Papazachos, Tectonophysics **28**, 213 (1975).
[22] C. H. Scholz, *The Mechanics of Earthquakes and Faulting* (Cambridge University Press, New York, 1994).
[23] J. Kaiser, Archiv für das Eisenhüttenwesen **24**, 43 (1953).
[24] I. G. Main and P. G. Meredith, Geophys. J. Int. **107**, 363 (1991).
[25] P. A. Cowie and C. H. Scholz, J. Struct. Geol. **14**, 1133 (1992).
[26] G. R. Irwin, in *Handbuch der Physik*, Vol. 6 (Springer-Verlag, Berlin, 1958), p. 551.
[27] P. C. Paris and G. C. Sih, in *Fracture Toughness Testing and Its Applications*, Vol. 381 (A.S.T.M. International, Conshohocken, PA, 1965), p. 30.